

Excitation mechanisms in a nonequilibrium helium plasma jet emerging in ambient air at 1 atm

Tam Nguyen, Eduardo Hernandez, Vincent M. Donnelly, and Demetre J. Economou

Citation: *Journal of Vacuum Science & Technology A* **36**, 04F406 (2018); doi: 10.1116/1.5023693

View online: <https://doi.org/10.1116/1.5023693>

View Table of Contents: <https://avs.scitation.org/toc/jva/36/4>

Published by the [American Vacuum Society](#)

ARTICLES YOU MAY BE INTERESTED IN

[Interferometry of plasma bursts in helium atmospheric-pressure plasma jets](#)

Journal of Vacuum Science & Technology A **36**, 04F402 (2018); <https://doi.org/10.1116/1.5023113>

[Atmospheric pressure plasma jet: A facile method to modify the intimal surface of polymeric tubular conduits](#)

Journal of Vacuum Science & Technology A **36**, 04F404 (2018); <https://doi.org/10.1116/1.5023259>

[Maghemite thin films prepared using atmospheric-pressure plasma annealing](#)

Journal of Vacuum Science & Technology A **36**, 04F405 (2018); <https://doi.org/10.1116/1.5023144>

[Estimating the number density and energy distribution of electrons in a cold atmospheric plasma using optical emission spectroscopy](#)

Journal of Vacuum Science & Technology A **36**, 04F407 (2018); <https://doi.org/10.1116/1.5023107>

[Perspective: The physics, diagnostics, and applications of atmospheric pressure low temperature plasma sources used in plasma medicine](#)

Journal of Applied Physics **122**, 020901 (2017); <https://doi.org/10.1063/1.4993710>

[Conversion of CO₂ in a packed-bed dielectric barrier discharge reactor](#)

Journal of Vacuum Science & Technology A **36**, 04F403 (2018); <https://doi.org/10.1116/1.5024400>

AVS Quantum Science

Co-published with AIP Publishing



Coming Soon!

Excitation mechanisms in a nonequilibrium helium plasma jet emerging in ambient air at 1 atm

Tam Nguyen, Eduardo Hernandez, Vincent M. Donnelly,^{a)} and Demetre J. Economou^{b)}
*Plasma Processing Laboratory, Department of Chemical and Biomolecular Engineering,
University of Houston, Houston, Texas 77204*

(Received 26 January 2018; accepted 1 June 2018; published 18 June 2018)

Species excitation mechanisms were studied, using optical emission spectroscopy, in a helium 200 kHz radio frequency (RF) plasma jet, emerging into the open air at 1 atm. The jet impinged on a dielectric substrate of either MgF₂ or quartz. Optical emissions between 115 and 950 nm were recorded through the substrate either along the jet axis or at a steep angle to isolate emissions originating from the region near the substrate surface. Time-resolved emission was observed close to the substrate surface only during a brief period near the positive peak of the applied RF voltage. No emission close to the substrate was observed during the negative voltage with the exception of a weak emission from N₂ ($C^3\Pi_u \rightarrow B^3\Pi_g$) just prior to the peak negative voltage. N₂⁺, H, O, OH, and NO emissions along the discharge axis, from impurities in the He feed, or air diffusing into the He jet just downstream of the end of the tube (nozzle), were dominated by Penning ionization of N₂ and dissociative excitation of water and O₂ by He metastables (He*). Unlike the fully modulated electron-impact excited emission from N₂ and He, emissions produced by collisions with He* were weakly modulated during the RF period and were shifted in phase with respect to the peak positive or peak negative voltage. This was attributed to vacuum ultraviolet emissions, in the radiation-trapped environment of atmospheric pressure, that produced He* outside the discharge tube even during the period when the plasma was confined inside the tube. N₂ emission revealed a weak ionization wave propagating during the positive voltage period, well before the peak positive voltage. At peak positive voltage, ionization and excitation in the gap between the nozzle and the substrate maximized. The plasma positively charged the substrate, resulting in the brief N₂ emission observed during the negative voltage period, as electrons drifted toward the substrate to neutralize the positive charge. *Published by the AVS.* <https://doi.org/10.1116/1.5023693>

I. INTRODUCTION

Atmospheric pressure, nonequilibrium low-temperature plasmas (LTPs) have gained much attention due to many current or potential applications.^{1–3} Compared to the traditional low pressure counterparts, atmospheric pressure LTPs do not require expensive vacuum systems and can operate in open air.⁴ Like their low pressure counterparts, atmospheric pressure LTPs have high electron temperature, while the gas is moderately above room temperature, allowing processing of thermally sensitive materials, including biological specimens. Different discharge configurations have been developed to combat issues such as arcing^{1,5} and to tailor the system to a particular application.¹

An important variant of atmospheric pressure LTPs is the atmospheric pressure plasma jet (APPJ). In this configuration, helium (or another inert gas, e.g., argon) flows through a small-diameter dielectric tube and a discharge is ignited inside the tube that can extend several centimeters from the tube exit (nozzle). A commonly found characteristic of APPJ is that the jet, despite appearing continuous to the naked eye, is in fact comprised of individual packets, or “plasma bullets,” generated by an ionization wave moving at high speed (10s–100s km/s), similar to streamers created by corona discharges.⁶ Unlike corona discharges, however, which create

streamers in unpredictable and nonrepeatable fashion, plasma bullets can be both predictable and repeatable.⁶

Various theories and models have been proposed in an attempt to explain the creation and propagation of plasma bullets.⁶ A model was developed⁷ based on the theory of streamers, or ionization waves,⁸ observed in corona discharges in point-plane or wire-plane gaps.⁶ In this cathode-directed streamer model, the luminous front is a ball of positive ions. Photons emitted by excited states ionize the gas in front of the streamer head. The strong local electric field pulls electrons toward the streamer head, causing an avalanche, while leaving behind positive ions. These positive ions become the new luminous front, while the electrons neutralize the previous ball of ions, resulting in a relatively dark channel behind the streamer head. The plasma bullet is theorized to propagate in a similar manner. Another type of streamer is the negative, or anode-directed streamer, in which electrons move in the same direction as the streamer. Negative streamers are usually shorter, move slower, and emit less light compared to positive streamers. Also, the tip of negative streamers is pointed, as opposed to the oval shape of positive streamers.⁶

For laminar gas flow conditions, the luminous jet of APPJs typically extends several centimeters beyond the nozzle. Placing an insulating substrate near the nozzle allows precise exposure of small regions of the surface to plasma bullets that then propagate radially along the surface before extinguishing.⁹ In pure carrier gas (usually He) APPJs,

^{a)}Electronic mail: vmdonnelly@uh.edu

^{b)}Electronic mail: economou@uh.edu

species generated by inward-diffusing ambient air react to form a variety of radicals and metastables in the plasma^{6,10} including various reactive oxygen-nitrogen species^{11,12} that have been shown to be important in many biological processes. Several aspects of the complex chemistry and physics of APPJs have been studied through experiments and modeling.^{5,6} The substrate surface is exposed to a plethora of radicals as well as metastables, low-to-moderate energy positive ions, high-energy photons, and electrons. These can react with the surface and generate volatile products that can then enter the plasma. Although significant progress has been made, the identities, fluxes, and energies of many important species in APPJs are still largely unknown.

In this study, time- and space-resolved optical emission spectroscopy (OES) was used to study a He APPJ emerging from a quartz tube in open air at 1 atm, and impinging on a dielectric substrate. Particular emphasis was placed on the region near the substrate surface. Near-surface emission was detected through two transparent substrates (MgF₂ and quartz) to cover the wavelength range from 115 to 950 nm. The spatial and temporal behavior of various emissions was used to study important species excitation mechanisms, as well as plasma jet evolution in the presence of a floating dielectric substrate.

II. EXPERIMENTAL APPARATUS AND PROCEDURES

In the APPJ used in this study, helium feed gas (99.999% purity) flowed through a quartz tube (5.5 mm inner diameter and 9.5 mm outer diameter) at 4 standard liters per minute. Two ring electrodes, each 13 mm long (measured along the tube axis), were wrapped around the tube 10 and 45 mm away from the tube end (nozzle). The upstream electrode was grounded, while the downstream electrode was powered by a 200 kHz, 7 kV_{p-p} peak-to-peak sinusoidal voltage waveform. The voltage supplied by a function generator (BNC model 645) was fed to a radio frequency (RF) power amplifier (ENI model 2100L). The output of the amplifier was connected to an inductor and then to the downstream ring

electrode. The voltage was measured by an oscilloscope (Tektronix TDS 2024B) through a 1000:1 voltage attenuator.

OES was performed in the ultraviolet/visible/near-infrared range of wavelengths (190–950 nm), with the jet impinging on the flat face of a half-cylinder quartz prism with semicircular cross section (Fig. 1). The nozzle was 20 mm away from the substrate surface. Light gathered from the curved side of the prism was focused onto the input of an optical fiber. Emission was detected as a function of angle θ_2 , as shown in Fig. 1. Time-averaged OES was carried out with four spectrometers (Ocean Optics, model HR4000), each with a predefined range of wavelengths. For time-resolved OES, an intensified charge-coupled device (ICCD, Princeton Instruments, model PI-Max I) was attached to a TRIAX 550 spectrometer. The ICCD was also used for time-resolved imaging of the overall (spectrally unresolved) plasma emission.

Light from the plasma impinging on the flat face of the prism at angle θ_1 with respect to the surface normal is passing through the prism at angle θ_2 , according to Snell's law, $n_1 \sin(\theta_1) = n_2 \sin(\theta_2)$, where $n_1 = 1$ and n_2 are the indices of refraction of the plasma gas (essentially empty space) and the prism material (quartz), respectively. For an average radius of the plasma jet cylinder (just before it spreads out on the surface), $r_p = 0.75$ mm, and small collection angle, the distance (d) away from the surface over which light is collected is given by $d = r_p / \tan \theta_1$ (Fig. 2), as $\theta_1 \rightarrow 90^\circ$, $d \rightarrow 0$, and $\theta_2 \rightarrow \theta_c$, the so-called critical angle. The index of refraction of quartz (n_2) is a (weak) function of wavelength over the range of interest.^{13,14} Using $\theta_2 = 40^\circ$, at 309 nm (OH peak), the corresponding $n_2 = 1.49$ and $d = 0.225$ mm. On the other hand, at 844 nm (O-atom peak), the corresponding $n_2 = 1.45$, and $d = 0.291$ mm. Figure 3 shows geometrical details of the optical setup. The prism diameter was 50 mm. The aperture diameter was 6 mm, placed 49 mm away from the curved side of the prism. A 5 mm lens was attached in front of the optical fiber, placed 51 mm away from the aperture. In addition, based on the geometry of the system, the light collection angle, for observation along the axis, was $\sim 1^\circ$ and $\sim 3^\circ$ for light at the nozzle and at the substrate, respectively.

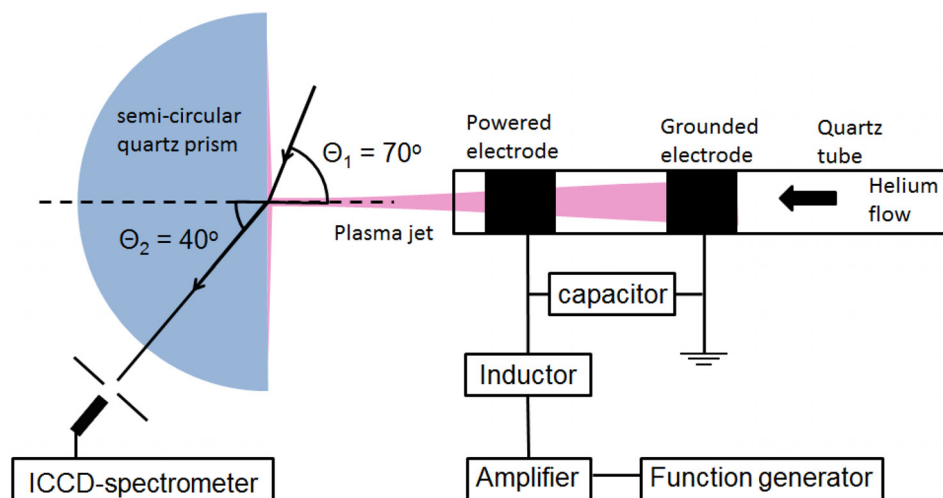


Fig. 1. (Color online) Experimental system (not drawn to scale) used for OES in the UV/visible/near-IR range.

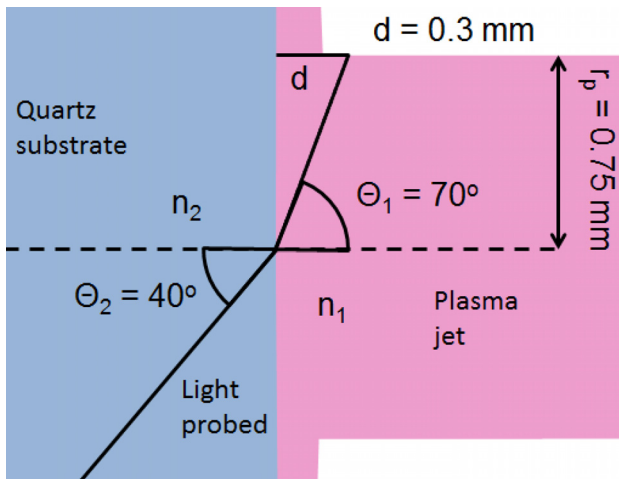


FIG. 2. (Color online) At an observation angle of $\theta_2 = 40^\circ$, and an average radial extent of the plasma on the substrate $r_p = 0.75$ mm, emission is probed from a region $d \sim 0.3$ mm away from the quartz substrate surface. θ_1 and θ_2 are related by Snell's law: $n_1 \sin(\theta_1) = n_2 \sin(\theta_2)$.

Detection of emissions in the vacuum-UV (VUV) range (115–200 nm) required a different spectrometer (McPherson 234/302 monochromator, with 789A-3 controller, and 658-1 photomultiplier tube, PMT) that was evacuated by an ion pump. The plasma impinged directly on a MgF_2 window that was sealed to the spectrometer in front of the entrance slit. Time-averaged analog PMT current was amplified with a pico-ammeter (Keithley 6485) and recorded on a computer. Time-resolved OES was recorded by dropping the PMT current across a $100\ \Omega$ resistor and measuring the voltage with an oscilloscope. The APPJ was positioned to detect light either on axis along the entire length of the discharge [Fig. 4(a)] or near the substrate surface only [Fig. 4(b)].

Additionally, emission spectra were obtained by detecting light passing through the quartz discharge tube walls, perpendicular to the tube axis and between the electrodes. In this configuration, emission from impurities in the He feed gas were unambiguously identified.

III. RESULTS

A. Plasma images

The plasma jet had a diameter of about 1.5 mm and extended (in the absence of a substrate) ~ 25 mm from the

nozzle in ambient air. Upon striking the dielectric surface, 20 mm from the nozzle, the plasma spread out radially. Time-resolved images of the jet taken with an ICCD are shown in Fig. 5.

The jet first appears shortly before the voltage reaches its maximum positive value. Then, the jet achieves maximum brightness (shown in Fig. 5, upper panel) and continues to persist well after the maximum positive voltage has passed. When the voltage is negative, a discharge can be seen in the tube, downstream from the powered electrode (Fig. 5, lower panel). This discharge becomes brightest as the voltage reaches near a maximum negative value. Unlike other studies,^{15–18} a clearly defined plasma bullet propagating from the tube to the substrate was not observed. Instead, when the jet appeared, it had already reached the substrate. This behavior will be explained later by looking at the time resolved emission of nitrogen.

B. Time-averaged spectra

Time-averaged emission was recorded along the axis, collected over the distance from the back of the discharge tube to the surface of the quartz prism or MgF_2 window. A typical set of spectra is shown in Fig. 6. It is comprised of spectra from five spectrometers that were stitched together and normalized to the same intensity over the overlapping wavelength ranges. Aside from the strongest He (706.5 nm) peak, emissions from H, O, N, $\text{OH}(A^2\Sigma^+ \rightarrow X^2\Pi)$, $\text{N}_2(C^3\Pi_u \rightarrow B^3\Pi_g)$, $\text{N}_2^+(B^2\Sigma_u^+ \rightarrow X^2\Sigma_g^+)$, and $\text{NO}(A^2\Sigma^+ \rightarrow X^2\Pi)$ were identified. The NO emission was very weak, requiring longer integration time with the Ocean Optics UV spectrometer to achieve an acceptable signal-to-noise ratio. Time-averaged spectra (not shown) were also recorded by collecting light through the quartz discharge tube wall (i.e., perpendicular to the axis). These spectra contained emission from He, and much weaker emissions from OH, O, H, N_2 , and N_2^+ , probably due to trace impurities in the helium feed. These emissions are not likely to come from ambient air species diffusing inside the tube against the helium flow. Due to the high Peclet number ($\text{Pe} = uL/D \sim 1800$, where u is the gas convective flow velocity, L is characteristic length scale, and D is diffusivity of air species in He), the flow is highly convective, and N_2 , O_2 , and water vapor from the ambient air can back-diffuse only a short distance (< 0.5 mm from the

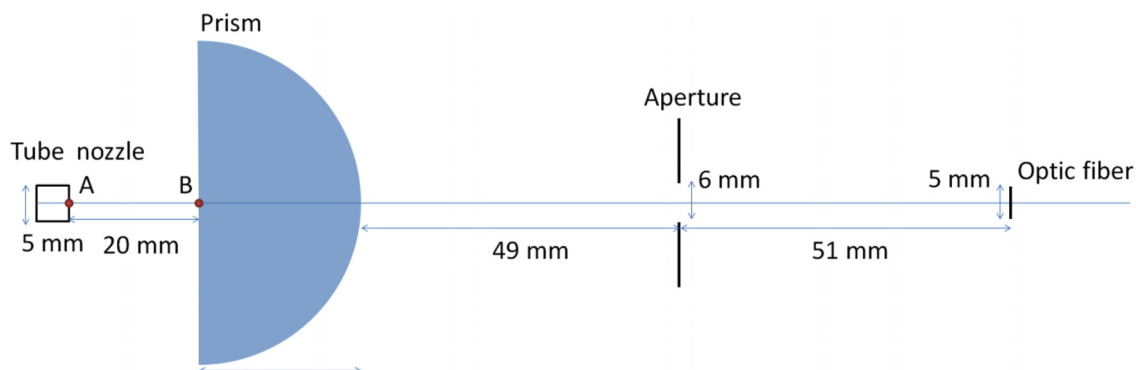


FIG. 3. (Color online) Geometric details of the optical setup. Collection angles at points A and B are $\sim 1^\circ$ and $\sim 3^\circ$, respectively.

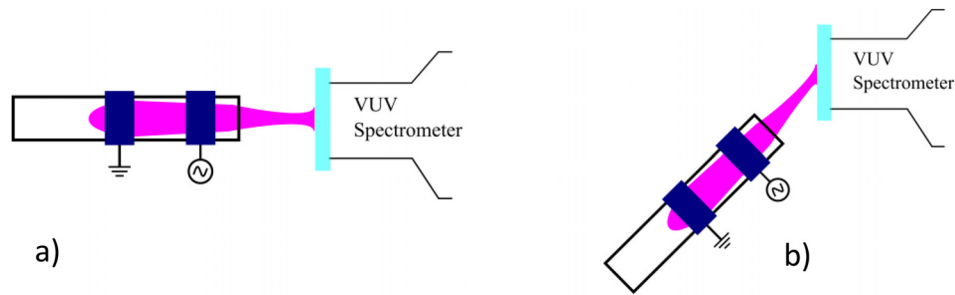


FIG. 4. (Color online) VUV spectrometer probing light from the plasma jet along the axis (a), or at angle (b), to isolate emission only from the surface of the substrate (MgF₂ window in this case).

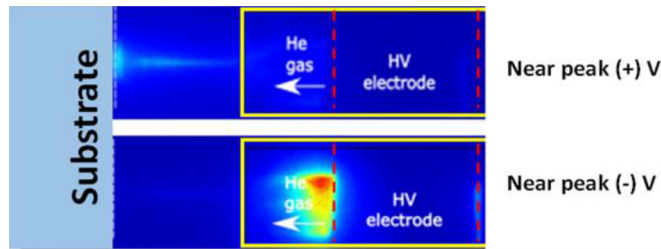


FIG. 5. (Color online) (not to scale) False color images of the plasma (10 ns exposure windows) 300 ns after the positive peak (top) or 100 ns after the negative peak (bottom) of the applied voltage. The internal boundary of the quartz discharge tube (near the nozzle) is indicated by the yellow box, and the high voltage electrode is located between the dashed red lines.

nozzle) into the tube. Thus, emissions recorded along the axis, except from He, were mainly due to species between the nozzle and the substrate, and/or impurities in the He feed gas.

Time-averaged spectra, presented in Fig. 7, were recorded at $\theta_2 = 20^\circ$ ($\theta_1 = 30^\circ$) to reject emission from inside the discharge tube and isolate emission from the plume near the quartz or MgF₂ surface. Spectra were stitched together in the same manner as in Fig. 6.

Signals were much lower, but all prominent emissions observed along the discharge tube axis in Fig. 6 are also found in Fig. 7. The relative intensities are quite different, however. Emission in the VUV from H Lyman- α and O were much weaker relative to UV-visible emissions, and

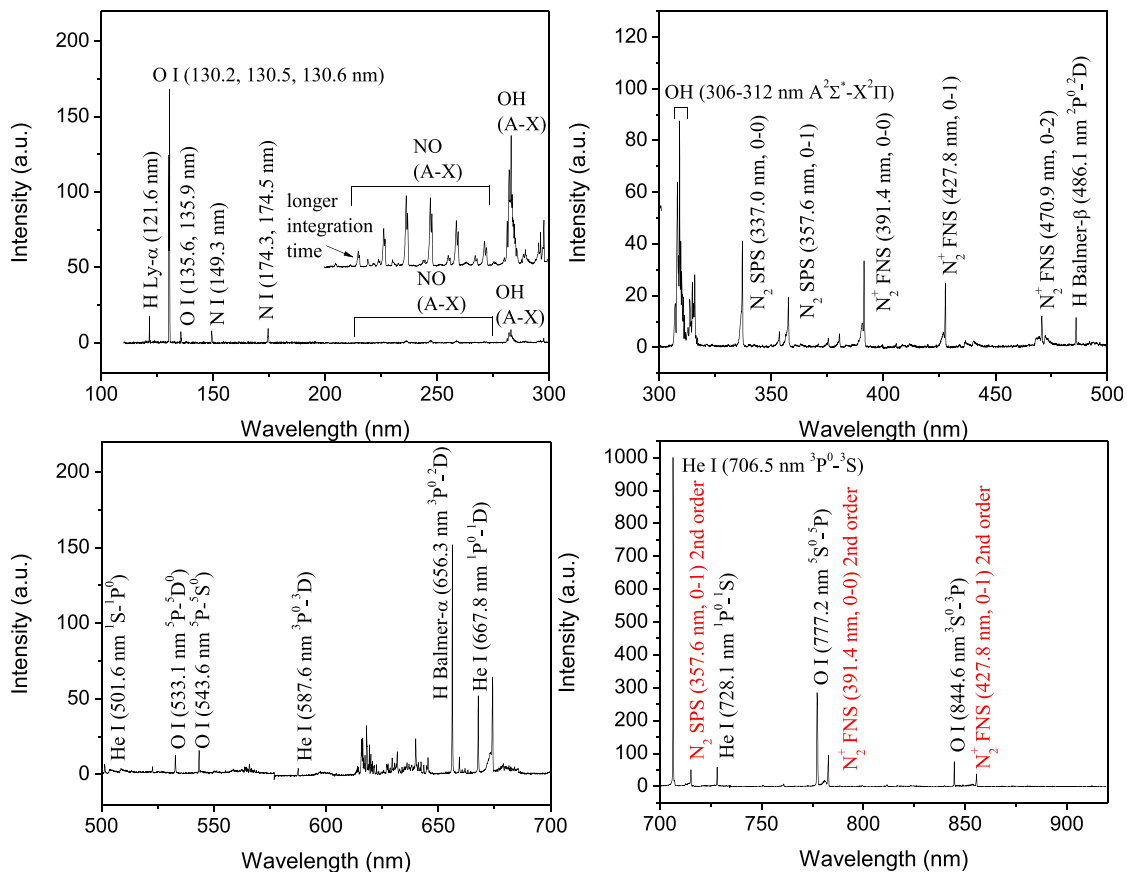


FIG. 6. (Color online) Typical emission spectra from 115 to 950 nm, recorded along the axis of the discharge ($\theta_1 = \theta_2 = 0^\circ$). Lines in parenthesis are second order peaks. The most intense peak was normalized to have an intensity of 1000.

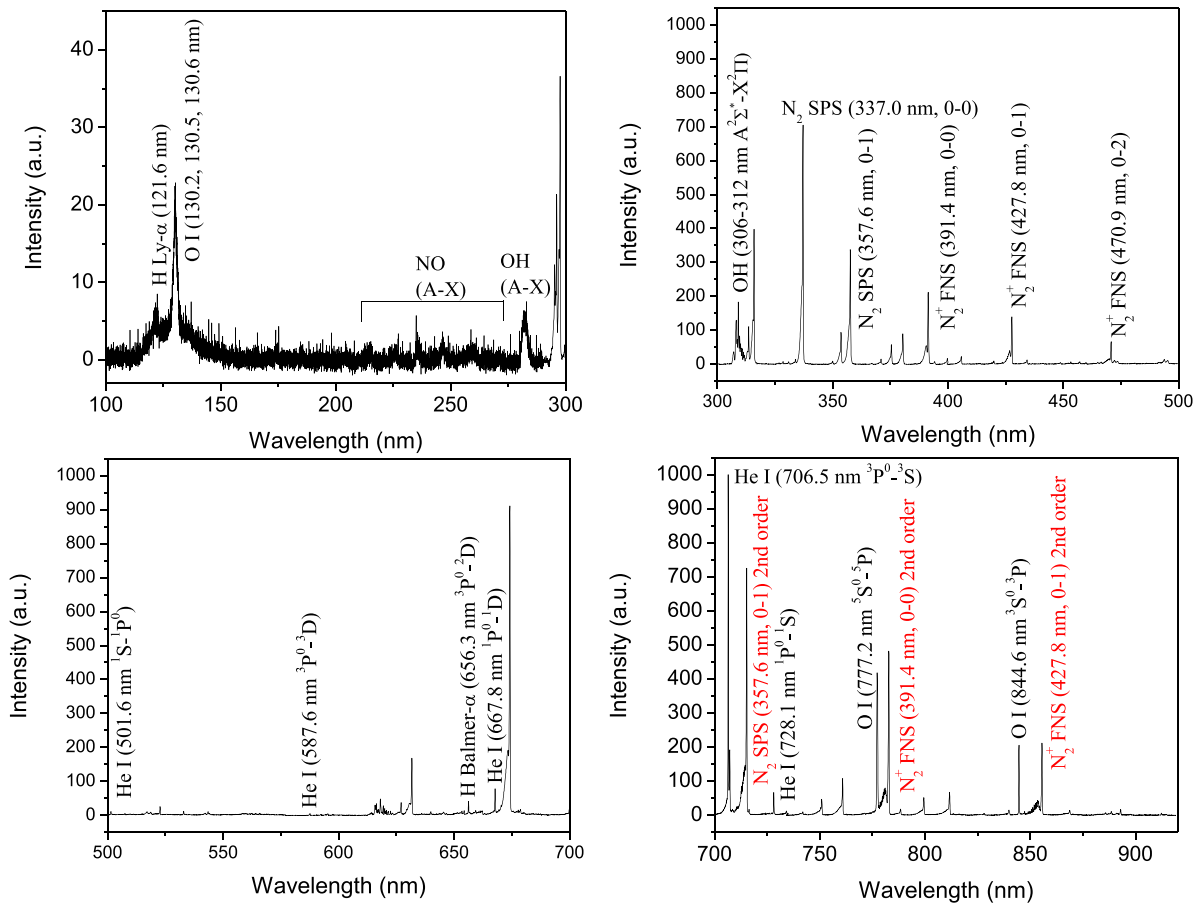


Fig. 7. (Color online) Typical emission spectra from 115 to 950 nm, recorded at an angle off of the discharge axis ($\theta_1 = 30^\circ$, $\theta_2 = 20^\circ$), thus looking at emissions near the substrate surface only. Lines in parenthesis are second order peaks. The most intense peak was normalized to have an intensity of 1000.

could only be detected by opening up the slits of the monochromator to ~ 1 mm. Emission from H Balmer- α was also relatively weak near the surface.

C. Time-resolved emission

Time-resolved emission over selected spectral lines was recorded with the ICCD-equipped spectrometer as a function of angle, at 50 ns increments throughout the RF cycle. The angle θ_2 (see Figs. 1 and 2) was varied from 0° to 40° . In Figs. 8–14, each time resolved emission intensity waveform is normalized to have a maximum of 1000. Time-resolved He 706.5 nm emission is presented in Fig. 8. The variation in angle θ_2 not only changes the axial position but also the radial position of the plasma being probed. At 0° , where light is detected from the plasma core of both the jet extending to the substrate surface and the plasma inside the tube, two broad peaks appear near the maximum positive and negative voltage, while very little emission is detected when the applied waveform is near zero volts. At 10° , the majority of emission is collected from the core region near the substrate and the outer edge of the plume a few millimeters along the radial direction. Some light from inside the tube is also collected, due to light that enters the prism 3 mm from its center and reaches the lens in front of the optical fiber leading to the spectrometer. Therefore, in view of the discharge structure shown in Fig. 5, the stronger peak at positive voltages is

due to the near-surface plasma. At 40° , light from both the edge and core region of the plasma close to the quartz prism surface is detected, and only a sharp peak at a maximum positive voltage appears. (It should be noted that whether light is collected from the core or the edge region of the plasma is of little consequence.)

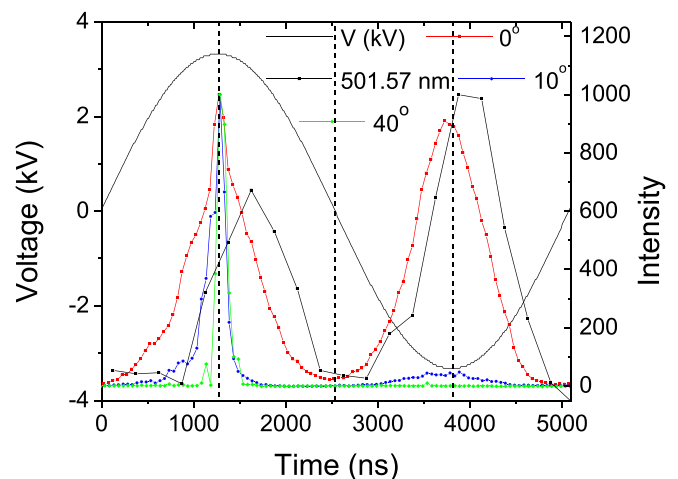


Fig. 8. (Color online) Time-resolved He (706.5 nm) emission at three different angles, θ_2 . The applied voltage waveform is shown. The time-resolved 501.57 nm line at $\theta_2 = 10^\circ$ is also shown. The vertical dashed lines are placed at peak positive and negative voltage, as well as zero voltage crossing.

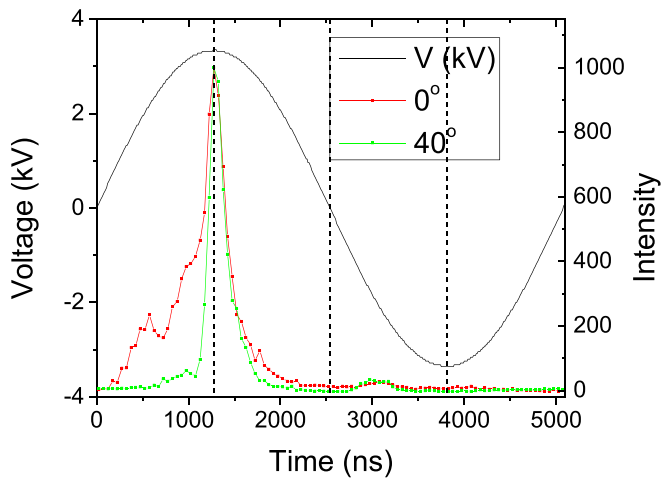


FIG. 9. (Color online) Time-resolved N_2 (337 nm) emission at $\theta_2 = 0^\circ$ and 40° . The applied voltage waveform is also shown. The vertical dashed lines are placed at peak positive and negative voltages, as well as zero voltage crossing.

It has widely been reported that an ionization wave travels to the substrate during the positive voltage portion of the RF cycle.^{5,6,16–21} The peak in He emission ~ 10 to 150 ns after the peak positive voltage, observed at 40° (also at angles of 20° and 30° , not shown), is expected to be due to electron impact excitation of He near the substrate surface (Fig. 5). There is a small time delay between the maximum voltage and the emission because it is possible for the ionization front to form before the voltage peaks, and reach the substrate surface about the same time the voltage reaches its maximum. The broad He emission peak observed at 0° throughout most of the negative voltage period arises from excitation in the plasma that is confined inside the discharge tube (Fig. 5). The 501.57 nm line shown in Fig. 8 is addressed in Sec. IV.

Time-resolved $N_2(C^3\Pi_u \rightarrow B^3\Pi_g)$ emission is shown in Figs. 9 and 10. Figure 9 shows sharp peaks near the peak

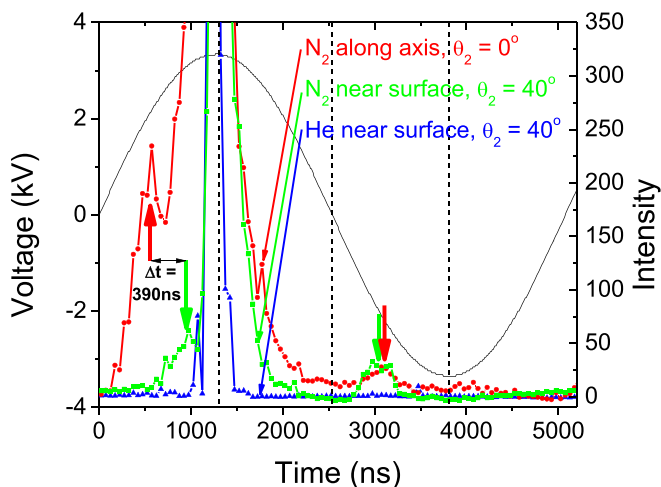


FIG. 10. (Color online) Time-resolved N_2 (337 nm) emission at $\theta_2 = 0^\circ$ and 40° showing expanded intensity scale of Fig. 9. The time-resolved He (706.5 nm) emission at $\theta_2 = 40^\circ$ is also shown. The vertical dashed lines are placed at peak positive and negative voltages, as well as zero voltage crossing.

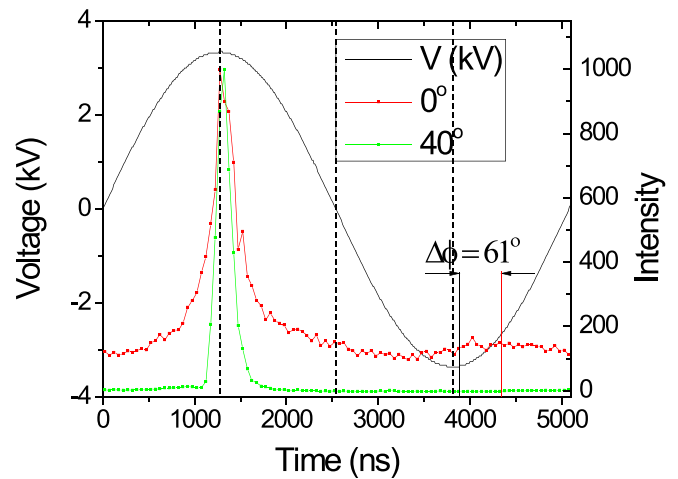


FIG. 11. (Color online) Time-resolved N_2^+ (391 nm) emission at $\theta_2 = 0^\circ$ and 40° . The applied voltage waveform is also shown. The phase shift, $\Delta\phi$, is based on the peak position of He (501.57 nm), assuming excitation occurs twice per RF (200 kHz) period. The vertical dashed lines are placed at peak positive and negative voltages, as well as zero voltage crossing.

positive voltage at 0° and 40° , similar to He 706.5 nm emission. This is ascribed to excitation, near the substrate surface, of nitrogen from the ambient air diffusing into the plasma jet. Upon closer inspection (Fig. 10), weak emission near peak negative voltage can be observed at both 0° and 40° . Furthermore, during the positive voltage portion of the cycle, before the strong emission near peak positive voltage, weaker peaks can be seen in Fig. 9 at both 0° and 40° . These features are explained in Sec. IV.

$N_2^+(B^2\Sigma_u^+ \rightarrow X^2\Sigma_g^+)$ 391 nm emission is shown in Fig. 11. At 40° , N_2^+ emission looks nearly the same as N_2 emission, minus the negative voltage peak, and is again attributed to excitation near the surface. At 0° , emission from N_2^+ is different than that from N_2 (and He) in that significant and weakly modulated emission is observed through the zero-voltage crossing and during the entire negative voltage fraction of the RF cycle.

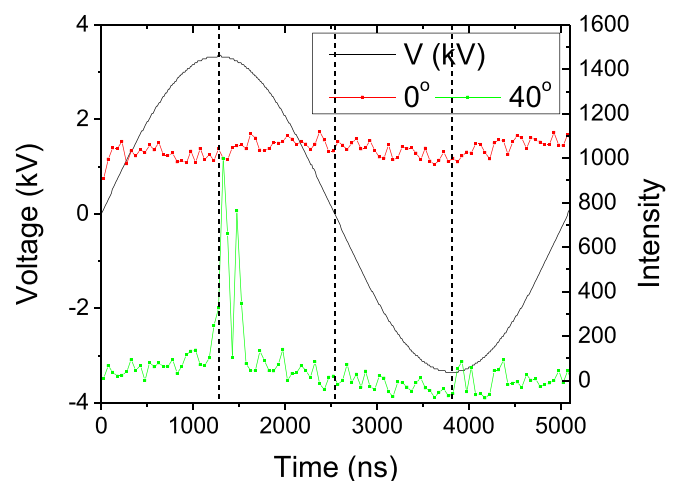


FIG. 12. (Color online) Time-resolved H (656 nm) emissions at $\theta_2 = 0^\circ$ and 40° . The applied voltage waveform is also shown. The vertical dashed lines are placed at peak positive and negative voltages, as well as zero voltage crossing.

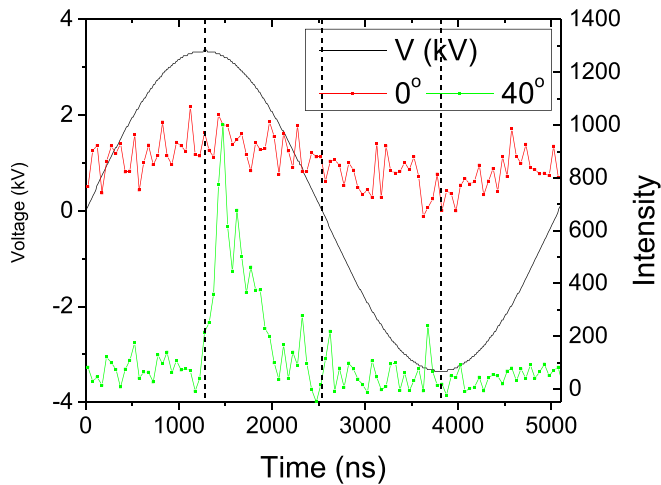


FIG. 13. (Color online) Time resolved OH (309 nm) emissions at $\theta_2 = 0^\circ$ and 40° . The applied voltage waveform is also shown. The vertical dashed lines are placed at peak positive and negative voltages, as well as zero voltage crossing.

Time-resolved emissions from H (656 nm), OH (309 nm), and O (844 nm) were also recorded. Measurements at 0° and 40° are shown in Figs. 12–14. At 40° , H and O emissions behave nearly the same as N_2 and He emissions, peaking sharply at or slightly past the peak positive voltage, again attributed to excitation near the surface. OH emission near the surface looks similar but is broadened during the decay to baseline at 2000 ns (vs 1600–1700 ns for H and O). At 0° , emissions from H and OH are found to be nearly constant throughout the period. O exhibits similar behavior with a small, sharp peak also found near the peak positive voltage.

Time-resolved VUV emissions (not shown) were also recorded, using the MgF_2 window as a substrate (Fig. 4). At 0° , H (122 nm) and O (130, 136 nm) emissions matched time-resolved emissions of the same species in the visible region; N (149 nm and 174 nm) emissions looked similar to H. Emissions from O (130 nm) was also recorded with the

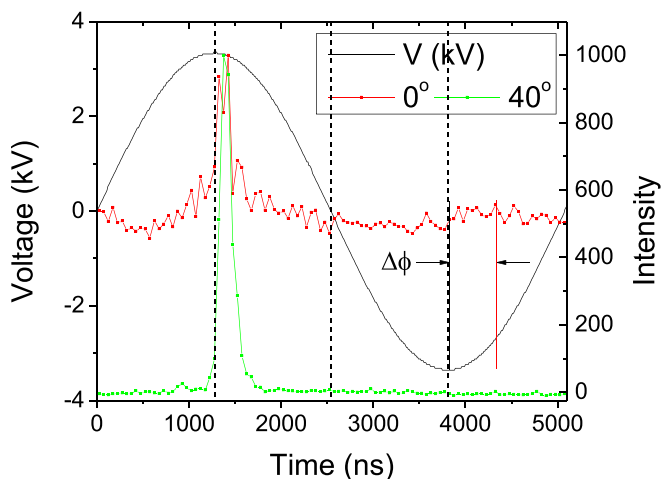


FIG. 14. (Color online) Time-resolved O (844 nm) emissions at $\theta_2 = 0^\circ$ and 40° . The applied voltage waveform is also shown. The vertical dashed lines are placed at peak positive and negative voltages, as well as zero voltage crossing.

plasma axis tilted so that emission from inside the discharge was blocked. At this $\sim 30^\circ$ angle, emission from the region close to the MgF_2 surface looked similar to O (844 nm) emission, peaking near the peak positive voltage.

IV. DISCUSSION

A. Excitation mechanisms

Helium emission can be excited by collisions of energetic electrons with the ground state He, as well as through collisions of lower energy electrons with He^+ or He “metastables” (He^*). (For these highly radiation-trapped conditions, we broaden the definition of metastables to encompass excited states with allowed transition to lower states, one of which can be the ground state. Such states would include those that emit in the VUV, in the 50–60 nm range.) Since the lifetimes of the excited states that emit at 706.5 and 501.57 nm are much shorter (36 and 75 ns, respectively) than the RF period (5 μ s), their time-resolved emission (Fig. 8) is representative of the time dependence of their electron impact excitation. The formation of He^* might be expected to follow a similar time dependence. Electron impact can create He^* directly, as well as through optical cascading from higher excited states. The latter process is enhanced by radiation trapping of VUV light at high pressure. The likely dominant $2p^1P^o \rightarrow ^1S$ He emission at 58.433 nm will be absorbed and re-emitted in the nozzle region 1000 times (on average) before decaying to the $2s^1S$ metastable state, emitting a 2058.1 nm photon in this cascade process. Collisions of N_2 with this metastable, as well as with $He(2p^1P^o)$ would produce $N_2^+(B^2\Sigma_u^+)$ emission. This radiation transport process can occur over roughly the distance of a tube diameter (5.5 mm) before the VUV photons random-walk out of the He flow stream. Experimental complexities precluded direct detection of the 58.433 nm He line, as well as the expected weaker lines at 53.703 and 52.221 nm from the $3p^1P^o \rightarrow ^1S$ and $4p^1P^o \rightarrow ^1S$ transitions, respectively. The detection of the 2058.1 nm line was also not possible with the current experimental setup. The analogous cascade emission by which the $3p^1P^o$ state decays into the same $2s^1S$ metastable state occurs at 501.57 nm and it is accessible. Although this is a very weak transition, we were able to detect it and found that it has a time dependence similar to that for He $3s^3S \rightarrow 2p^3P$ emission at 706.5 nm (see Fig. 8). There does appear to be a small time lag in the decay of the 501.57 nm emission with respect to the 706.5 nm emission, causing it to peak slightly past the peak negative voltage. While the precise cause for this difference is unknown, it likely has to do with the very different electron energy dependences of the cross sections for excitation (directly and through optical cascade transitions) of the triplet states responsible for the 706.5 nm and the singlet states giving rise to the 501.57 nm emissions. Helium has a 1S ground state; hence, electron impact transitions to triplet states are optically forbidden. This results in large cross sections near threshold and vanishingly small cross sections a few electron-volts above the threshold. On the other hand, optically allowed transitions to singlet states have a slower

rise above the threshold and then a more constant cross section up to several times threshold.²² In fact, the reason that the 706.5 nm line is so strong relative to the 501.57 emission is that cross sections for excitation of the upper triplet levels by electron impact excitation out of the metastable levels are extremely large and have much lower threshold energies.²³ Hence, if higher energy electrons are relatively more prominent later in the rf half periods, it would lead to a lag in 501.57 nm emission, relative to 706.5 nm emission, as observed. As discussed below, since singlet states produce VUV light that we believe is responsible for a slightly modulated production of He* in the plume that emerges from the discharge tube, we feel that the time-dependence of the 501.57 nm line is more representative of the production of He* than is the 706.5 nm line.

The energy of He metastables is sufficient to produce all other emissions observed in this study through multiple pathways. For this to occur, however, the excess energy must be released. For example, production of $v'=0$ $N_2(C^3\Pi_u)$ through collisions with He metastables would release a large amount of translational energy ($19.8 - 11.0 = 8.8$ eV), requiring an unreasonably large attractive force between He* and ground state N_2 . Even third body collisions are very unlikely during the short time of close interaction of He* and N_2 (of the order of half a vibrational period). Hence, all excitation of $N_2(C^3\Pi_u)$ is a result of electron impact.

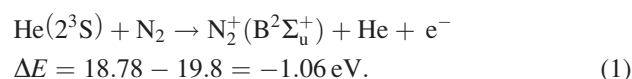
Figure 9 indicates that no N_2 emission is observed along the discharge axis during most of the negative voltage portion of the RF cycle. The time-resolved He emission detected at $\theta = 0$ during positive voltages consists of a broad feature on which is superimposed a weaker sharp peak near peak positive voltage. The sharp feature is likely ascribed to emission at the surface because it has the same shape as emission observed at $\theta = 40^\circ$ near maximum positive voltage, while the broad feature has a shape similar to that observed at $\theta = 0$ during negative voltages. One expects nearly equal plasma density and electron energy distributions during the positive and negative voltage periods in these types of dielectric barrier discharges. It is therefore reasonable to assume that the broad emission during negative voltages is a result of electron impact inside the tube. Since N_2 C-state is excited by electron impact and no N_2 emission is observed during the negative voltage period, then it follows that there is very little N_2 inside the tube, and the much weaker peaks before the peak negative voltage (Figs. 9 and 10) are due to electron impact in the region between the nozzle and the substrate surface (i.e., outside the tube). This was also confirmed by noting that very little N_2 emission was found in spectra of light transmitted through the quartz tube wall (perpendicular to the axis) between the electrodes.

During the positive voltage period, the intensity of N_2 emission observed along the discharge axis first rises in a similar manner to He emission, but then decays more rapidly than does the He emission (compare Figs. 8 and 9). Since plasma extends along the axis during this time, the slowly rising emission is attributed mainly to excitation in the emerging jet near the discharge tube-air boundary during

rising positive voltage, while the rapidly decaying emission later in the positive voltage period, behaving in a manner similar to He emission at the surface ($\theta_2 = 40^\circ$ in Fig. 8), comes mainly from electron impact excitation of N_2 near the substrate surface. This is also supported by the similar decay rate in N_2 emission observed at 0° and 40° during the period of falling positive voltage (Fig. 9).

During the negative voltage period, there is a small amount of emission from N_2 , over a small time window before the voltage reaches its peak negative value (Fig. 10). No other species exhibits such a feature. This is ascribed to a weak discharge that briefly develops near the substrate surface. Due to low electron temperature, as evident by the lack of He emission, this discharge cannot ionize He. As such, the discharge must be sustained by ionization of N_2 and O_2 , little He^+ and He* are formed, and no electron impact excitation of He emission or He*-induced emissions occurs during this time.

Time-resolved emission along the discharge axis from $N_2^+(B^2\Sigma_u^+)$ behaves differently from that of neutral N_2 (compare Figs. 9 and 11). During the positive voltage, a feature similar to that observed for the N_2 C-state appears to be superimposed on a background emission that persists throughout the negative voltage cycle. The background emission can be ascribed to Penning ionization



Unlike N_2 C-state excitation, in the production of $N_2^+(B^2\Sigma_u^+)$, the translational motion of the electron can take up the excess energy of 1.06 eV. The role of He metastable states in exciting certain species in atmospheric pressure plasmas has been explored.^{17,24,25} Xiong *et al.* showed that Penning ionization by He metastable states is responsible for the N_2^+ (391 nm) and the O (777 nm) spectral lines.¹⁷ Furthermore, N_2 was shown to play an important role in the propagation of the ionization wave by acting as the ion source through Penning ionization by He metastables.

Since the radiative lifetime of $N_2^+(B^2\Sigma_u^+)$ is short (60 ns) and $N_2^+(B^2\Sigma_u^+)$ is formed by collisions with He*, the observed time dependence of $N_2^+(B^2\Sigma_u^+)$ emission is proportional to the number density of He*. It was established that the plasma is confined inside the tube during the negative voltage period, and that N_2 originates from air diffusing into the plasma jet, but not into the tube due to high Peclet number. In that case, N_2 cannot reach the plasma inside the tube during the negative voltage to be ionized by He*. One possibility is He*, transported out of the tube by the gas flow, excite N_2^+ in the air. He* is created by electron impact on He. This occurs twice per RF period in the discharge between the two electrodes. Since the gas residence time between the electrodes is about 3000 times the RF period, each plug of gas passing through the discharge and exiting the nozzle would not be expected to produce a significant quantity of He* with a modulated number density. If we assume this flow of He* out of the nozzle to be the main source of N_2^+ excitation, then the $N_2^+(B^2\Sigma_u^+)$ emission

would not exhibit the modulation during the negative voltage seen in Fig. 11.

Another possibility for producing modulated He* is radiation transport. Each RF cycle produces two bursts of He emission through electron impact. How much this emission is modulated depends on the lifetime of the emitting states. The VUV emissions in the 50–60 nm range have very short radiative lifetimes (i.e., 0.5 ns for the $2p^1P^o$ state). This light is severely radiation-trapped at atmospheric pressure, but it is doubtful that its lifetime could be lengthened to durations comparable to the RF period. The photons are absorbed and re-emitted as they move out of the nozzle, where they produce $2p^1P^o$ He that would decay into the $2s^1S$ metastable state. As argued above, the 501.57 nm line ($3p^1P^o \rightarrow 2s^1S$) is expected to closely follow the creation of He* through this process. A $\Delta\phi = 61^\circ$ phase shift of the N_2^+ emission peak (Fig. 11) with respect to the peak He* excitation (proportional to 501.57 nm emission intensity, Fig. 8) can be used to estimate a lifetime for $N_2^+(B^2\Sigma_u^+)$ of $\tau_\phi = 0.72 \mu\text{s}$ (from $\tan \Delta\phi = \omega_e \tau_\phi$)²⁶ where the angular excitation frequency (ω_e) is twice the RF angular frequency, ω (here $\omega = 2\pi \times 200 \text{ kHz}$), and a sinusoidal excitation function with a period of ω_e is assumed.

A lifetime, $\tau_m = [(m/\alpha)^2 - 1]^{1/2}/\omega_e = 2.7 \mu\text{s}$, was also determined from the degree of modulation (α/m) ,²⁶ where m and α are the DC offset and the amplitude of the emission waveform, respectively, and the sinusoidal excitation function is assumed to have a DC level equal to its amplitude (i.e., the minima equal zero). The apparent discrepancy between τ_m and τ_ϕ can be explained as follows: Since the flow of He emerging from the discharge produces a continuous background of He*, the degree of modulation will be less than that expected if all He* were produced by VUV light. Therefore, the observed τ_m should be longer than τ_ϕ , and τ_ϕ is the true lifetime, since the phase shift is not a function of the degree of modulation of the excitation function.

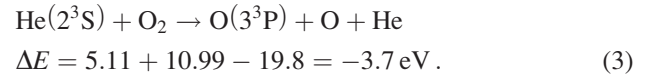
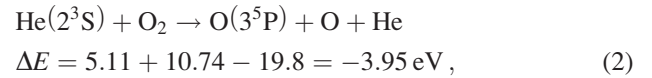
Assuming radiation transport for creation of He* near the nozzle, the $0.72 \mu\text{s}$ lifetime derived above would then correspond to the rate at which He* is destroyed by quenching collisions with the in-diffusing air very near the nozzle. If we equate He* with He($2s^1S$), it is lost through quenching collisions with N_2 and O_2 with rate constants of 1.7×10^{-10} and $5.8 \times 10^{-10} \text{ cm}^3 \text{ s}^{-1}$, respectively, near room temperature.²⁷ [Similar rate constants of 0.8×10^{-10} and $3 \times 10^{-10} \text{ cm}^3 \text{ s}^{-1}$ have been reported for quenching of He($2s^3S$) by N_2 and O_2 , respectively.²⁸] Then, the observed $0.7 \mu\text{s}$ lifetime would correspond to quenching by a partial pressure of 185 mTorr of air near the nozzle. Two-dimensional laminar flow (Navier-Stokes equations) and mass transfer computations of ambient air mixing with the helium jet in the open space between the nozzle and the substrate showed that air reaches a partial pressure of 185 mTorr on the jet axis ($r=0$) at an axial distance of $\sim 10 \text{ mm}$ from the nozzle. Hence, the conclusions drawn from the time dependent emission from $N_2^+(B^2\Sigma_u^+)$ along the axis seem reasonable.

$N_2^+(B^2\Sigma_u^+)$ can also be created directly through photoionization by the He VUV emission at 58.443 nm and several

other nearby lines. The cross section for production of this state is $2 \times 10^{-18} \text{ cm}^2$ at this wavelength.²⁹ Since the $N_2^+(B^2\Sigma_u^+)$ lifetime is very short, if the moderately modulated emission in the negative voltage half of the RF cycle (Fig. 10) were mainly due to this process, then the waveform and $2.7 \mu\text{s}$ lifetime derived from it would be representative of an unreasonably long VUV emission lifetime. Hence, it seems doubtful that generation of $N_2^+(B^2\Sigma_u^+)$ by photoionization plays a major role.

N_2^+ emission probed at $\theta_2 = 40^\circ$ was used to determine the lifetime of He* near the surface. A plot of the log of N_2^+ emission intensity versus time (Fig. 15) reveals a single exponential decay over 3 orders of magnitude, corresponding to a lifetime of 100 ns. This is longer than the N_2^+ B-state radiative lifetime of 60 ns, as well as the decay time for He emission, which is expected to be characteristic of the He* formation rate. Consequently, we ascribe the 100 ns decay time to the loss rate of He* near the surface. If He* is lost mainly by collisions with air, this corresponds to an air partial pressure of 2.5 Torr if He($2s^3S$) dominates or 1.3 Torr if He($2s^1S$) dominates. Both of these are very close to the partial pressure of 2.0 Torr computed (by two-dimensional fluid flow and mass transfer simulations) for air at the stagnation point on the substrate surface, again supporting the mechanisms presented here.

Time-dependent emission along the discharge axis from O at 844 nm (Fig. 14) was very similar to N_2^+ emission, including an identical decay rate of $\sim 100 \text{ ns}$ in the period following peak positive voltage (not shown), suggesting an analogous mechanism for the long-lived emission.



Production of O(3^5P) or O(3^3P) by collisions with He* can again be ruled out because the excess energy cannot be

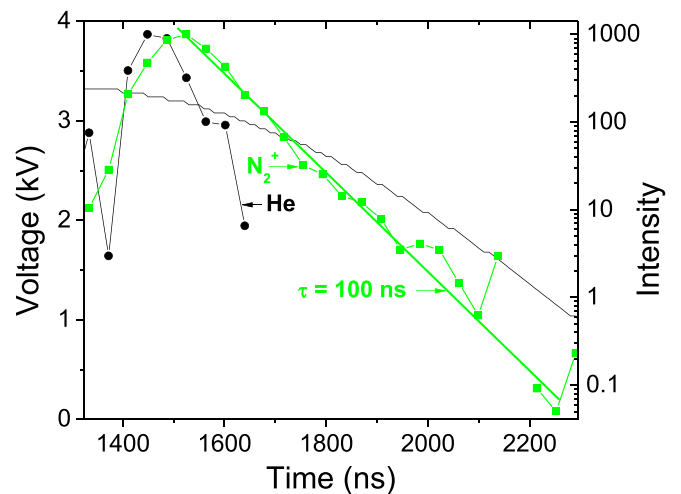
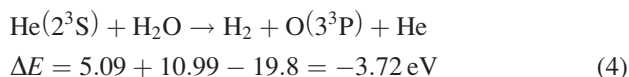


Fig. 15. (Color online) Decay of N_2^+ and He emission at the substrate surface. Part of the applied voltage waveform is also shown.

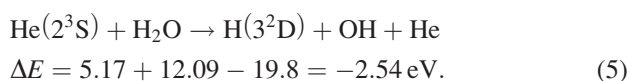
released. It is also possible, though less likely, to produce O emission through dissociation of H₂O, either directly



or through a two-step process with OH as the intermediary.

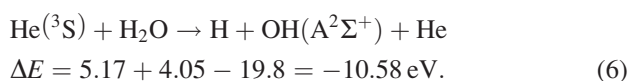
Unlike emission from He, N₂, N₂⁺, and O, time-resolved emissions from H (Fig. 12) and OH (Fig. 13) along the discharge axis exhibit no sharp peaks at the peak positive voltage and are barely modulated. This can be explained as follows. Unlike these other cases, emissions from H along the discharge axis originates from an impurity (i.e., H₂O or H₂) that is in the He feed gas at a high enough concentration that emission from inside the tube dominates that from outside the tube, including at the substrate surface. This is also confirmed by the observation that H and OH emission is substantial in the light passing through the quartz wall of the discharge tube. (In fact the H-to-He and OH-to-He emission ratios of this spectrum are larger than those observed along the discharge tube axis.) The feed gas was He (99.999%), thus, this emission is produced by at most 10 ppm of H₂O, and probably far less of H₂ in the feed gas.

H and OH emissions are excited by He* rather than by electron impact, as indicated by the lack of strongly peaked emission near the peak positive or negative voltage, found in the case of He emission (Fig. 8). As in the case of N₂ and O, collisions of He* with H cannot produce emission, because there is no way to release the excess energy. Instead these emissions are produced by dissociation of molecular species. The most likely pathway is through dissociation of H₂O



The lifetime of H Balmer- α emission is very short (2.3 ns), hence the emission lifetime is the lifetime of He*, inside the tube. No clear phase shift can be determined from the waveform (it appears close to 90°). A more reliable estimate of the lifetime can be obtained from the degree of modulation, which appears to be ~ 0.04 (Fig. 12), giving a lifetime of $\sim 10 \mu\text{s}$. This is much shorter than the time for metastable diffusion to the discharge tube walls ($\sim 0.1 \text{ s}$) and could be due to quenching of metastables by H₂O, metastable pooling or collisions with electrons.

Finally, OH emission along the discharge axis also exhibits no sharp peaks and a low degree of modulation (Fig. 13), indicating that it is excited by He*. The most likely precursor is again water



The time dependence of OH emission appeared to be somewhat different than H emission in that it peaked modestly, slightly after peak positive voltage. This perhaps indicates

that some of the OH emission is due to reactions outside the discharge tube.

When probed at 40°, time-resolved emissions from all species except OH showed a sharp peak at maximum positive voltage, when the jet reached the quartz prism. Helium emission reflects the period over which energetic electrons can cause dissociative excitation directly, as well as create He*, which in turn can cause dissociative excitation. The sharp peaks observed in species other than OH are due to the short lifetime of electrons and He* when exposed to ambient air. OH emission would likely have behaved the same way if not for the 700 ns lifetime of the OH(A²Σ⁺) state, and the apparent lack of quenching by He or air, resulting in a noticeable tail in OH emission.

B. Aspects of plasma jet evolution

The N₂ emission (Fig. 10) can also be used to gain an understanding of how the plasma jet evolves. Compared to He, N₂ requires lower energy electrons to be excited. As such, N₂ emission tracks lower energy electrons, while He emission tracks higher energy electrons. When looking either along the axis ($\theta_2 = 0^\circ$) or at $\theta_2 = 40^\circ$, a small peak (arrows on the left side of Fig. 10) before the main peak is observed. This feature does not exist in He emission, indicating that this small peak is the result of lower energy electrons that cannot excite He. There is a 390 ns time lapse between the peak seen along the axis (red arrow on the left side of Fig. 10) and when it appears at the substrate (green arrow on the left side in Fig. 10). We conclude that this corresponds to an ionization wave traveling (on average) $2 \text{ cm} / (390 \times 10^{-9} \text{ s}) = 5 \times 10^6 \text{ cm/s}$, ionizing (and exciting) the gas on its way. An ionization channel then forms between the tube and the substrate as peak positive voltage is reached, with the substrate acting as the counter electrode.³⁰ The plasma during the positive voltage charges the substrate positively.³¹

When the powered electrode swings into negative voltage, electrons exiting the discharge inside the tube drift toward the substrate to neutralize the positive charge, causing the weak emission seen near the surface (at 40°), 700 ns before the peak negative voltage. Electrons exiting the nozzle travel a distance of 2 cm to the substrate during the 500 ns time lapse between the zero voltage crossing and the appearance of the emission peak (Fig. 10). Given the electron mobility in He, [$10^6 \text{ cm}^2/\text{kV s}$ (Ref. 32)] at 300 K and 1 atm, the electric field required for electrons to travel 2 cm in 500 ns is 4 kV/cm, comparable to that measured by Sretenović *et al.*³³ This emission appears at the same time whether light is probed at 40° or along the axis (at 0°), and therefore, only occurs near the surface. This can be explained by the increase in electric field strength versus distance from the nozzle³⁴ and the higher concentration of N₂ near the substrate.

V. SUMMARY AND CONCLUSIONS

An atmospheric pressure plasma jet in helium emerging from a quartz tube in open air at 1 atm was studied using optical emission spectroscopy. Two copper rings, a 200 kHz RF electrode and a grounded electrode were wrapped around

the tube. Gas exiting the tube impinged on a dielectric substrate comprised of either a MgF₂ window sealed to a vacuum UV spectrometer, or the flat face of a half-cylinder quartz prism with semicircular cross section. Time-resolved (over the RF cycle) and time-averaged emissions were recorded through the substrate either along the discharge axis, or at a steep angle to isolate emission originating from the region near (<0.3 mm) the substrate surface.

Time-resolved emission was observed close to the substrate surface only during a brief period near the positive peak of the applied RF voltage. No emission was observed near the surface during the negative voltage with the exception of a weak emission from N₂(C³Π_u → B³Π_g, 337 nm) just prior to the peak negative voltage. Along the discharge axis, helium emission (706.5 nm) was from both outside and inside the discharge, while emission from H (656 nm), O (777 and 844 nm) and OH (309 nm) was mostly from inside the discharge. N₂ emission along the axis appeared to originate from the entire length of the jet that extended from the nozzle to the substrate surface during positive voltage.

Emissions along the discharge axis, due to impurities originating from either the He source or air diffusing into the He jet, were dominated by dissociative excitation by He metastables (He*). Axial emission from N₂⁺ (391 nm) was also produced by collisions with He* (i.e., Penning ionization of N₂). In particular, N₂⁺ emission was observed even during the negative voltage part of the cycle when there was no jet propagating into the open air that could produce He* to excite N₂⁺. This may be explained by radiation transport. At atmospheric pressure, He VUV emissions in the 50–60 nm range were radiation-trapped, causing them to be absorbed and re-emitted as they moved out of the nozzle and produced 2p¹P⁰ He that would decay into the 2s¹S metastable state.

Unlike electron-impact excited emission from N₂ and He, emissions produced by collisions of He* with N₂, O₂ and H₂O were only modulated to a small degree during the RF period, and were shifted in phase with respect to the peak positive or negative voltage.

Time-resolved emissions from He, N₂, and N₂⁺ also provided insight on the formation and evolution of the plasma jet. Helium emission tracked the number density of higher energy electrons, while N₂ emission tracked the number density of lower energy electrons. N₂ time-resolved emission revealed a weak ionization wave propagating during the positive voltage part of the cycle, but well before the peak positive voltage. This wave only excited N₂ (and not He) due to the relatively low electron energy. Ionization and excitation in the gap between the nozzle and the substrate maximized when the voltage reached its peak positive value. After the positive voltage portion of the cycle the insulating substrate charged positively, leading to a brief emission from N₂, during the negative voltage portion of the cycle, as electrons drifted toward the substrate to neutralize the positive charge.

ACKNOWLEDGMENTS

The authors are grateful to the Department of Energy (Office of Fusion Energy Science, Contract No. DE-SC0001939) for financial support of this work. Thanks are due to Peng Lin for carrying out the fluid flow and mass transfer computations.

- ¹C. Tundero, C. Tixier, P. Tristant, J. Desmaison, and P. Leprince, *Spectrochim. Acta*, **B 61**, 2 (2006).
- ²O. V. Penkov, M. Khadem, W. S. Lim, and D. E. Kim, *J. Coat. Technol. Res.* **12**, 225 (2015).
- ³D. Mariotti and R. M. Sankaran, *J. Phys. D: Appl. Phys.* **43**, 323001 (2010).
- ⁴A. Schutze, J. Y. Jeong, S. E. Babayan, J. Park, G. S. Selwyn, and R. F. Hicks, *IEEE Trans. Plasma Sci.* **26**, 1685 (1998).
- ⁵X. Lu, M. Laroussi, and V. Puech, *Plasma Sources Sci. Technol.* **21**, 034005 (2012).
- ⁶X. Lu, G. V. Naidis, M. Laroussi, and K. Ostrikov, *Phys. Rep.* **540**, 123 (2014).
- ⁷X. Lu and M. Laroussi, *J. Appl. Phys.* **100**, 063302 (2006).
- ⁸G. A. Dawson and W. P. Winn, *Z. Phys.* **183**, 159 (1965).
- ⁹W. Yan and D. J. Economou, *J. Appl. Phys.* **120**, 123304 (2016).
- ¹⁰T. Murakami, K. Niemi, T. Gans, D. O'Connell, and W. G. Graham, *Plasma Sources Sci. Technol.* **22**, 015003 (2013).
- ¹¹J. Ehlbeck, U. Schnabel, M. Polak, J. Winter, T. von Woedtke, R. Brandenburg, T. von dem Hagen, and K. D. Weltmann, *J. Phys. D: Appl. Phys.* **44**, 013002 (2011).
- ¹²J. S. Sousa, K. Niemi, L. J. Cox, Q. T. Algwari, T. Gans, and D. O'Connell, *J. Appl. Phys.* **109**, 123302 (2011).
- ¹³I. H. Malitson, *J. Opt. Soc. Am.* **55**, 1205 (1965).
- ¹⁴C. Z. Tan, *J. Non-Cryst. Solids* **223**, 158 (1998).
- ¹⁵B. L. Sands, B. N. Ganguly, and K. Tachibana, *Appl. Phys. Lett.* **92**, 151503 (2008).
- ¹⁶J. J. Shi, F. C. Zhong, J. Zhang, D. W. Liu, and M. G. Kong, *Phys. Plasmas* **15**, 013504 (2008).
- ¹⁷Q. Xiong *et al.*, *J. Appl. Phys.* **106**, 083302 (2009).
- ¹⁸N. Puac, D. Maletic, S. Lazovic, G. Malovic, A. Dordevic, and Z. L. Petrovic, *Appl. Phys. Lett.* **101**, 024103 (2012).
- ¹⁹G. V. Naidis, *Appl. Phys. Lett.* **98**, 141501 (2011).
- ²⁰C. Jiang, M. T. Chen, and M. A. Gundersen, *J. Phys. D: Appl. Phys.* **42**, 232002 (2009).
- ²¹Z. Xiong, X. Lu, Y. Xian, Z. Jiang, and Y. Pan, *J. Appl. Phys.* **108**, 103303 (2010).
- ²²R. M. Stjohn, C. C. Lin, and F. L. Miller, *Phys. Rev.* **134**, A888 (1964).
- ²³D. L. A. Rall, F. A. Sharpton, M. B. Schulman, L. W. Anderson, J. E. Lawler, and C. C. Lin, *Phys. Rev. Lett.* **62**, 2253 (1989).
- ²⁴W. C. Zhu, Q. Li, X. M. Zhu, and Y. K. Pu, *J. Phys. D: Appl. Phys.* **42**, 202002 (2009).
- ²⁵K. Niemi, J. Waskoenig, N. Sadeghi, T. Gans, and D. O'Connell, *Plasma Sources Sci. Technol.* **20**, 055005 (2011).
- ²⁶L. F. Keyser, S. Z. Levine, and F. Kaufman, *J. Chem. Phys.* **54**, 355 (1971).
- ²⁷A. L. Schmeltekopf and F. C. Fehsenfeld, *J. Chem. Phys.* **53**, 3173 (1970).
- ²⁸T. P. Parr, D. M. Parr, and R. M. Martin, *J. Chem. Phys.* **76**, 316 (1982).
- ²⁹J. A. R. Samson, G. N. Haddad, and J. L. Gardner, *J. Phys. B—At. Mol. Opt.* **10**, 1749 (1977).
- ³⁰Q. T. Algwari and D. O'Connell, *IEEE Trans. Plasma Sci.* **39**, 2368 (2011).
- ³¹Y. Ito, Y. Fukui, K. Urabe, O. Sakai, and K. Tachibana, *Jpn. J. Appl. Phys.* **49**, 066201 (2010).
- ³²A. V. Phelps, J. L. Pack, and L. S. Frost, *Phys. Rev.* **117**, 470 (1960).
- ³³G. B. Sretenović, I. B. Krstić, V. V. Kovacevic, B. M. Obradovic, and M. M. Kuraica, *J. Phys. D: Appl. Phys.* **47**, 102001 (2014).
- ³⁴A. Sobota *et al.*, *Plasma Sources Sci. Technol.* **25**, 065026 (2016).